

A 3D discontinuous Galerkin finite element method with the bond-based peridynamics model for dynamic brittle failure analysis

B. Ren, C.T. Wu, Y. Guo, W. Hu, Y.C. Wu

Livermore Software Technology Corporation, 7374 Las Positas Road, Livermore, CA 94551

1 Abstract

Peridynamics is a new nonlocal theory that provides the ability to represent displacement discontinuities in a continuum body without explicitly modelling the crack surface. In this paper, an explicit dynamics implementation of the bond-based peridynamics formulation is presented to simulate the dynamic fracture process in 3D elastic solid. Based on the variational theory, the Discontinuous Galerkin (DG) approach is utilized to formulate the classic peridynamics governing equation. As a result, the spatial integration can be carried out through finite element approach to enforce the boundary conditions, constraints, contacts as well as to handle the non-uniform mesh in the engineering practices. The classic material parameters, such as the elastic modulus and fracture energy release rate are employed for the determination of material response and failure in brittle material. Several numerical benchmarks are conducted to invest the convergence and mesh sensitivity of simulations of dynamic crack propagation process with different refinements. The results demonstrate that the proposed peridynamics formulation can capture the 3D dynamic crack process in brittle material effectively and accurately including multi-crack nucleation, propagation and branching.

Keywords: Bond-Based Peridynamics, Discontinuous Galerkin, Finite Element Method

2 Introduction

The numerical simulation of material failure is a longstanding challenge in the computational mechanics society as well as in the industry. The main difficulty arises from the incompatibility between the physical discontinuities emerging from material failure and the partial differential equations utilized by the classic continuum mechanics theory to describe the material response of a solid body. Another numerical difficulty of the material failure simulation in solids is the challenge of maintaining an adequate data structure representing the evolving crack surfaces during failure process. Much effort has been devoted to overcome these numerical challenges. At the continuum level, the XFEM method [1] introduces the level set method into the finite elements and implicitly determines the position and orientation of crack tips. However, as a mesh-based method, a sophisticated book-keeping algorithm is required to track the crack surface which turns out to be very difficult in 3D problems. The Cohesive FEM [2] method can naturally represent the evolving discontinuity in computational domain. However, cohesive laws in the cohesive model are phenomenological which not only ruins the consistency of the material property but also leads to a convergence problem even in an isotropic solid. The meshfree methods [3] also have been developed to model the material failure. Compared to the XFEM, the meshfree methods update the connectivity with customized approximations and represent the moving boundary conditions with less effort. However, the current techniques to handle multiple cracks seem to not be robust and require further research. On the other hand to avoid the localization issue and thus the mesh sensitivity issue, the nonlocal theories which have been developed since the late of 1970s [4] are used in XFEM and meshfree methods. To evade the spatial differential operation nearby crack surface, the continuum weakly or strictly nonlocal models [5] have been developed. These models lead to a formulation where the spatial derivatives in the weak form of corresponding governing equations are smeared along the material failure surfaces.

Peridynamics is one of the nonlocal methods proposed by Silling [6,7]. It has been considered as a viable and efficient numerical method for the material and structural failure problems. Peridynamics theory replaces the spatial differential term in the classical mechanical theories by a nonlocal integral term that assembles the interaction forces of a material point with its neighbors. The first peridynamics model was presented in 1997. It was named bond-based peridynamics and was applied to the brittle

materials [6]. In the bond-based peridynamics model, each material point interacts with its neighbors in a compact zone. The interaction between two material points is called a “bond” which is independent with each other. The pair-wise bond forces are collinear with the line of a bond and have opposite directions. The bond-based peridynamics model is well-developed and has been applied to the simulation of damage and fracture in the brittle materials [8], the reinforced concrete materials [9], the composite laminate structures [10], the brazed joints [11] and geo-materials [12]. The three-dimensional formulas of the bond-based peridynamics can be derived from a pair-wise elastic potential model which shall result in a constant Poisson’s ratio $\nu = 0.25$ rooted in the so-called Cauchy relation, i.e., the elastic modulus tensor satisfies the relations as $D_{1122} = D_{1212}$. To address this restriction, the so-called ordinary and non-ordinary state-based peridynamics models [13,14] were proposed in which the bond forces are dependent each other in contrast with that in the bond-based peridynamics. The state-based peridynamics evaluates the bond force based on the multi-body potential function which has the capability to represent both the effect of volume and shear. Although the state-based peridynamics model has the potential to solve the general material failure problems, it is still an ongoing research topic. There are some technical issues [15, 16] remain to be further discussed.

The motivation of the peridynamics theory is the prediction of material damage in a 3D solid. Thus the peridynamics computational space is firstly partitioned by a set of material particles. Subsequently, the nonlocal integral term of peridynamics theory is implemented by the nodal integral approach [17]. This meshfree type of implementation can capture the crack path freely. However, the boundary condition enforcement cannot follow the standard way of the meshfree Galerkin formulations. Another shortcoming is that the accuracy of computation decays dramatically in the case of non-uniform discretization. An alternative way to perform the spatial integration and avoid those numerical defects in peridynamics models is constructing an approximation field of the kinematic quantity by finite element (FE) shape function [18, 19]. Based on this argument, the integration operation can be carried out through Gauss integration points. Several studies [20, 21] have been conducted to verify that the peridynamics model can be implemented in the FEM framework with nonlocal boundary conditions. The FEM peridynamics approach inherits the advantages of FEM method such as the straightforward boundary condition enforcement and the robustness in non-uniform discretization. To represent the strong discontinuities in FEM peridynamics, the continuous approximation field is replaced by a piecewise continuous field which results in a discontinuous Galerkin formula for peridynamics [19, 22, 23] in quasi-static analysis. The piece-wise continuous approximation implies the capability to represent the crack surfaces automatically. The research reports [22, 23] indicate that this model can lead to a stable solution for the quasi-static problems.

Instead of modeling brittle fracture as a quasi-static problem, this paper presents the explicit dynamics bond-based peridynamics formulas using the FEM discontinuous Galerkin theory for the dynamic fracture problems. A distributive micro modulus of each bond is calculated from the classic elastic modulus to enforce an equivalent elastic energy density from the peridynamics and continuum mechanics theory. This paper is organized as follows. In section 2, the basic bond-based peridynamics formulations are reviewed. Section 3 constructs the 3D dynamic discontinuous Galerkin weak form of the bond-based peridynamics model. The relations between the nonlocal peridynamics quantities and classic mechanics quantities are derived based on the equivalent elastic energy density in Section 4. After that, several benchmark problems are presented in Section 5. Final remarks are given in Section 6.

3 The bond-based peridynamics model

The bond-based peridynamics model can be considered a macro-scale molecular dynamics model. The dynamic motion of a peridynamics point is governed by the collective of the interaction forces of this point and its neighboring points in a compact zone. The equation of motion of any point (\mathbf{X}) at reference configuration at time t is:

$$\rho \ddot{\mathbf{u}} = \int_{H_X} \mathbf{f}(\mathbf{u}(\mathbf{X}', t) - \mathbf{u}(\mathbf{X}, t), \boldsymbol{\xi}) dV_{X'} + \mathbf{b}(\mathbf{X}, t), \quad (1)$$

where H_X is a compact neighborhood zone of \mathbf{X} , named as horizon. The horizon of \mathbf{X} is defined as $H_X = \{\mathbf{X}' | |\mathbf{X}' - \mathbf{X}| \leq \delta\}$, where δ is the radius of a sphere centered at \mathbf{X} . $\boldsymbol{\xi}$ denotes a bond as $\boldsymbol{\xi} = \mathbf{X}' - \mathbf{X}$. The pair of interaction forces (\mathbf{f}) between \mathbf{X} and \mathbf{X}' is collinear with the bond and has opposite orientation which is determined by the relative displacement of two points: $\boldsymbol{\eta} = \mathbf{u}(\mathbf{X}', t) - \mathbf{u}(\mathbf{X}, t)$. \mathbf{b} is the prescribed body force density. The integration term in Eq. (1) collects all the bond forces imposed to \mathbf{X} .

There are two important hypothesizes of the bond force: (1) the bond force is a short range force, i.e., it only appears inside the compact zone:

$$\mathbf{f}(\boldsymbol{\eta}, \boldsymbol{\xi}) = 0 \text{ when } |\boldsymbol{\xi}| > \delta. \quad (2)$$

\mathbf{f} is a pairwise interaction force satisfying:

$$\mathbf{f}(-\boldsymbol{\eta}, -\boldsymbol{\xi}) = -\mathbf{f}(\boldsymbol{\eta}, \boldsymbol{\xi}), \quad (3)$$

which ensures the conservation of linear momentum [14].

In the bond-based peridynamics model, the material is considered as *microelastic* implying that a bond force is related to a *micropotential* w :

$$\mathbf{f}(\boldsymbol{\eta}, \boldsymbol{\xi}) = \frac{\partial w(\boldsymbol{\eta}, \boldsymbol{\xi})}{\partial \boldsymbol{\eta}}, \quad (4)$$

where the *micropotential* is a peridynamics concept which is a measurement of the elastic energy stored in a bond. In contrast to that of classic continuous mechanics, the *micropotential* has the unit of N/m^5 . Consequently, the bond force $\mathbf{f}(\boldsymbol{\eta}, \boldsymbol{\xi})$ has the dimension of N/m^6 . The energy density of \mathbf{X} can be collected through all its bonds:

$$W = \frac{1}{2} \int_{H_X} w(\boldsymbol{\eta}, \boldsymbol{\xi}) dV_{X'}. \quad (5)$$

The governing equation of the bond-based peridynamics is constructed from the derivative of energy equation. Here the formations of $w(\boldsymbol{\eta}, \boldsymbol{\xi})$ represent the material types. It can be linear, non-linear isotropic or anisotropic materials. This paper employs the *prototype microelastic brittle* (PMB) material model [15]. The PMB model is a linear isotropic material model in which each bond is considered as a linear spring. The *micropotential* of a PMB bond is evaluated from the stretch of a bond:

$$w(|\boldsymbol{\eta}|, |\boldsymbol{\xi}|) = \frac{1}{2} cs^2 |\boldsymbol{\xi}|, \quad (6)$$

where c is the spring constant named as *microelastic* modulus. s is the bond stretch ratio:

$$s = \frac{|\boldsymbol{\xi} + \boldsymbol{\eta}| - |\boldsymbol{\xi}|}{|\boldsymbol{\xi}|}. \quad (7)$$

In the case of small deformation, the bond force is calculated as:

$$\mathbf{f}(\boldsymbol{\eta}, \boldsymbol{\xi}) = cs \frac{\boldsymbol{\xi}}{|\boldsymbol{\xi}|}. \quad (8)$$

The bond-based peridynamics model captures the material failure by a bond-based failure criterion: the critical bond stretch (s_c) [14, 15]. With this failure model, a bond with stretch above s_c will be broken and this breakage is irreversible. It is said that a crack surface will be formed when all bonds crossing this surface are broken. Under this hypothesis, the critical stretch is related to classic fracture mechanics quantity: energy release rate, G_c [14, 15]. In the 3D case, this relation is given as:

$$G_c = \frac{\pi cs_c^2 \delta^5}{10}. \quad (9)$$

Unlike the local damage mechanics models, there is no explicit damage indicator in the peridynamics model. The failure is introduced at the bond level which is a nonlocal status. However, a local damage indicator of a point can be defined through the status of its bonds [14, 15]:

$$D(\mathbf{X}) = 1 - \frac{\int_{H_X} \varphi(\boldsymbol{\xi}) dV_{X'}}{\int_{H_X} dV_{X'}}, \quad (10)$$

where:

$$\varphi(\boldsymbol{\xi}) = \begin{cases} 1, & \text{for } s(\boldsymbol{\xi}) < s_c \\ 0, & \text{otherwise} \end{cases} \quad (11)$$

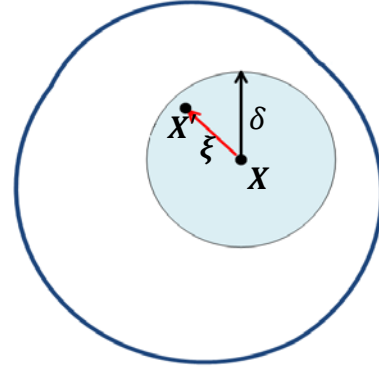


Fig. 1. The peridynamics model.

4 The Discontinuous Galerkin weak form

The computational domain of a peridynamics problem is denoted as Ω with essential boundary condition S_u . The solution of this problem is located in a subspace of Banach space: $S(\Omega) = \{\mathbf{u}(\mathbf{X}) \in L^2(\Omega) | \mathbf{u}(\mathbf{X}_g) = g(\mathbf{X}_g) \forall \mathbf{X}_g \in S_u\}$. Let $\mathbf{v}(\mathbf{X})$ denote a test function located at $S'(\Omega) = \{\mathbf{v}(\mathbf{X}) \in L^2(\Omega) | \mathbf{v}(\mathbf{X}_g) = 0 \forall \mathbf{X}_g \in S_u\}$. The Galerkin weak form of problem of Eq. (1) is posed as:

$$\int_{\Omega} \rho \ddot{\mathbf{u}}(\mathbf{X}) \cdot \mathbf{v}(\mathbf{X}) dV_X = \int_{\Omega} \int_{H_X} \mathbf{f}(\boldsymbol{\eta}, \boldsymbol{\xi}) dV_{X'} \cdot \mathbf{v}(\mathbf{X}) dV_X + \int_{\Omega} \mathbf{b}(\mathbf{X}) \cdot \mathbf{v}(\mathbf{X}) dV_X$$

$$\forall \mathbf{u}(\mathbf{X}) \in S(\Omega), \mathbf{v}(\mathbf{X}) \in S'(\Omega). \quad (12)$$

Like the regular FEM method based on the continuous Galerkin method, the approximation fields of the solution ($\mathbf{u}(\mathbf{X})$) and test function ($\mathbf{v}(\mathbf{X})$), are constructed based on the FEM shape function given by:

$$u_i(\mathbf{X}) = u_i^A N^A(\mathbf{X}), \quad v_i(\mathbf{X}) = v_i^A N^A(\mathbf{X}), \quad (13)$$

where u_i^A denotes the nodal displacement u_i of node A. Using the notation in Eq.(13), the index form of Eq. (12) can be organized in the following equation for discretization:

$$\int_{\Omega} \rho \ddot{u}_i^A N^A(\mathbf{X}) N^B(\mathbf{X}) dV_X = \int_{\Omega} \left(\int_{H_X} f_i(\boldsymbol{\eta}, \boldsymbol{\xi}) dV_{X'} \right) N^B(\mathbf{X}) dV_X + \int_{\Omega} b_i(\mathbf{X}) N^B(\mathbf{X}) dV_X. \quad (14)$$

In the discretization of the continuous FEM domain, the adjacent elements share nodes whereas each element has its own nodes in that of the discontinuous FEM domain, i.e., the total nodal number equals the total element number times the node number per element. Eq. (14) contains two levels of integration. The first level of integration is the computational domain integration discretized by the summation of Gaussian points like the regular FEM integration:

$$\sum_{g=1}^{ng} \rho N^B(\mathbf{X}^g) \Delta V^g \ddot{u}_i^B = \sum_{g=1}^{ng} \left(\int_{H_X} f_i(\boldsymbol{\eta}(\mathbf{X}^g), \boldsymbol{\xi}(\mathbf{X}^g)) dV_{X'} \right) N^B(\mathbf{X}^g) \Delta V^g + \sum_{g=1}^{ng} b_i(\mathbf{X}) N^B(\mathbf{X}^g) \Delta V^g, \quad (15)$$

where ng denotes the total number of Gaussian points in the domain. The row-sum mass matrix treatment is used in the left side of Eq. (15) for the explicit dynamics simulation. The integration remaining in Eq. (15) represents the nonlocal effect of a Gaussian point \mathbf{X}^g . Because the first level of integration is carried out through Gaussian points, the bond connectivity in the domain is build up based on the Gaussian points system. This treatment leads to:

$$\begin{cases} \boldsymbol{\xi}(\mathbf{X}^g) = N^A(\mathbf{X}^g) \mathbf{X}^A - N^{A'}(\mathbf{X}^{g'}) \mathbf{X}^{A'} \\ \boldsymbol{\eta}(\mathbf{X}^g) = N^A(\mathbf{X}^g) \mathbf{u}^A - N^{A'}(\mathbf{X}^{g'}) \mathbf{u}^{A'} \end{cases} \quad (16)$$

where $\boldsymbol{\xi}(\mathbf{X}^g)$ is a bond between Gaussian point \mathbf{X}^g and its neighbor Gaussian point $\mathbf{X}^{g'}$ in its horizon. Therefore the integration domain in Eq. (15) which is a sphere centered at \mathbf{X}^g can be discretized by Gaussian points. Finally the discretized bond-based explicit dynamics peridynamics governing equation becomes:

$$\sum_{g=1}^{ng} \rho N^B(\mathbf{X}^g) \Delta V^g \ddot{u}_i^B =$$

$$\sum_{g=1}^{ng} \left(\sum_{g'=1}^{ng'} f_i(\boldsymbol{\eta}(\mathbf{X}^g, \mathbf{X}^{g'}), \boldsymbol{\xi}(\mathbf{X}^g, \mathbf{X}^{g'})) \Delta V^{g'} \right) N^B(\mathbf{X}^g) \Delta V^g + \sum_{g=1}^{ng} b_i(\mathbf{X}^g) N^B(\mathbf{X}^g) \Delta V^g, \quad (17)$$

where ng' is the total number of neighbors of \mathbf{X}^g . $\mathbf{X}^{g'}$ can exist crossing elements. N^B is the FEM shape function. For each Gaussian point, \mathbf{X}^g , B loops all the nodes of its element and will eventually loop all the nodes in the mesh after all Gaussian points (ng) are calculated. Because the approximation field is constructed by regular FEM shape function, the boundary conditions can be enforced by the standard FEM way. The boundary effect of the nonlocal constitutive law will be corrected in the sense of equivalent elastic energy density throughout the domain and as further described in the next section.

In the forgoing derivation, the integration-by-parts theory plays no role in the variational FEM formulation and therefore no derivative terms are present which making the DG method a perfect fit for peridynamics to simulate the fracture process.

5 The equivalent classic mechanics quantities for PMB material

As discussed in Section 2, there are only two material quantities which characterize a PMB material: the microelastic modulus c and the critical bond stretch s_c . These two quantities are not ordinary

material constants used in the classic mechanics models, such as elastic modulus and Poisson's ratio. Fortunately, the microelastic modulus and critical bond stretch can be related to classic mechanics quantities based on the equivalent strain energy in the continuous mechanics sense. It's known that the Poisson's ratio of a PMB is restricted to 0.25 in 3D case. In contrast with other peridynamics implementations in which a constant modulus c is used throughout PMB, this work calculates the distributive c for each Gaussian point to enforce an equivalent elastic energy density in PMB. The classic elastic energy density inside a solid under small deformation condition is defined as:

$$U = \frac{1}{2} \boldsymbol{\sigma} : \boldsymbol{\epsilon}, \quad (18)$$

where $\boldsymbol{\sigma}$ is the Cauchy stress tensor and $\boldsymbol{\epsilon}$ is engineering strain tensor. This expression can be expanded as:

$$U = \frac{\nu\mu}{1-2\nu} (\epsilon_{xx} + \epsilon_{yy} + \epsilon_{zz})^2 + \mu (\epsilon_{xx}^2 + \epsilon_{yy}^2 + \epsilon_{zz}^2) + \mu (\epsilon_{xy}^2 + \epsilon_{yz}^2 + \epsilon_{zx}^2), \quad (19)$$

Here, ν, μ are the Poisson's ratio and shear modulus respectively. For the isotropic deformation ($\epsilon_{xx} = \epsilon_{yy} = \epsilon_{zz} = \epsilon$, $\epsilon_{xy} = \epsilon_{yz} = \epsilon_{zx} = 0$) condition, the elastic energy density is ($\nu = 0.25$):

$$U = 3E\epsilon^2, \quad (20)$$

where E is the elastic modulus. For the case of uniaxial deformation ($\epsilon_{xx} = \epsilon$, $\epsilon_{yy} = \epsilon_{zz} = \epsilon_{xy} = \epsilon_{yz} = \epsilon_{zx} = 0$), the elastic energy density can be calculated as:

$$U = \frac{3}{5} E\epsilon^2. \quad (21)$$

The analytical integration of Eq. (5) under the assumptions of spherical horizon and isotropic deformation is derived to build up the relation between c and E . [14, 15]

$$c = \frac{18k}{\pi\delta^4}. \quad (22)$$

However, this relation decays nearby boundary and under non-uniform discretization. In this work, the elastic energy density of a Gaussian point is enforced to equal the collective energy density of all its bonds under isotropic deformation condition which results in ($\epsilon = s$):

$$3E = \sum_{\xi} \frac{1}{2} c_X |\xi| \Delta V_{X'}. \quad (23)$$

Eq. (23) indicates that the microelastic modulus c_X is a distributive quantity in contrast with a constant parameter throughout PMB domain in other peridynamics models. In other words, c_X depends on the discretization (coarse or fine, uniform or non-uniform) as well as the location of X . The points nearby boundary have bigger c_X than that located inside domain because the boundary X has fewer bonds. Theoretically, Eq. (23) requires a linear equation solver to find the solution of c_X . In practice, the analytical solution Eq. (22) can be considered as the initial solution and a couple of iterations in the implicit solving will lead to an accurate estimation of solution for c_X . Using Eq. (3), the bond force with this distributive elastic modulus becomes

$$\mathbf{f}(\boldsymbol{\eta}, \boldsymbol{\xi}) = \frac{c_X + c_{X'}}{2} s \frac{\boldsymbol{\xi}}{|\boldsymbol{\xi}|}. \quad (24)$$

Eq. (23) ensures the equivalent elastic energy density under isotropic deformation. The equivalence for the other deformation status is not granted. For that reason, an ellipsoid calibration algorithm [14] is utilized to adjust the elastic modulus of a point to fit the complex stress status. The horizon of a point X is a sphere with radius δ . Assume a surrounding point X' has the spherical coordinates (r, ϕ, θ) , as shown in Fig. 2. In a specific mesh, an artificial uniaxial deformation along X-axis is defined: $x_1(t) = X_1 + aX_1$, $x_2(t) = X_2$, $x_3(t) = X_3$, here x_i denotes the coordinate at current configuration. a is the deformation along X-axis. We choose $a = 0.001$ as an initial guess. In this case, the ratio between real elastic energy density (Eq. (21)) and the collective bond energy density (Eq. (6)) can be calculated by

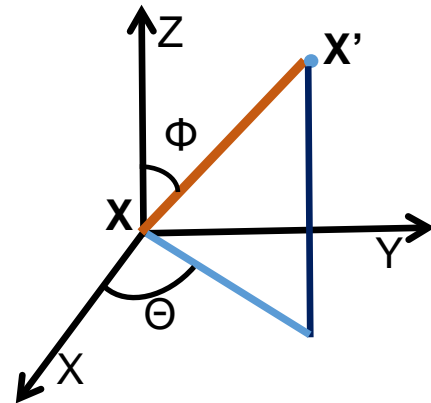


Fig. 2. The sphere coordinates of a bond

$$T_1 = \frac{\frac{3}{5}Ea^2}{\sum_{\xi} \frac{1}{4}(c_X + c_{X'})|\xi|\Delta V_{X'}}. \quad (25)$$

With the same process, the ratio between real elastic energy density and the collective bond energy density along Y- and Z- axis can be evaluated as T_2, T_3 respectively. T_i is an orientation dependent vector while the microelastic modulus is a scalar. Here an ellipsoid algorithm is adopted to construct a scalar factor to calibrate the microelastic modulus with respect to uniaxial deformations [14]:

$$c_c = \sqrt{\left(\frac{1}{(\cos(\theta)\sin(\phi))^2} + \frac{1}{(\sin(\theta)\sin(\phi))^2} + \frac{1}{(\cos(\phi))^2}\right)}. \quad (26)$$

Eventually, the microelastic modulus was corrected as:

$$c_X = c_c c_X^0, \quad (27)$$

where c_X^0 is the value estimated by Eq. (23). Note that the numerical equivalence procedure described in this section only needs to be performed once in the initialization phase and not needed during the time-marching stage for a dynamic simulation.

6 Numerical examples

In this section, five benchmark examples are presented to study the performance of the discontinuous Galerkin bond-based peridynamics formulas and numerical algorithm. The numerical time integration of the discrete equation (Eq. (17)) is performed by the central difference integration algorithm[29]. The standard bilinear shape function of 8 nodes elements with 8 Gaussian points each element is used for all examples. For all numerical examples, the horizon radius $\delta = 0.8 * l_e$ (l_e : the diagonal length of each element), which implies that δ is a distributive value in a computational domain. The convergences of δ and Gaussian points number are not discussed in this paper. However, they can be a reasoned conclusion from the result of Section 5.2 and 5.3.

6.1 The wave propagation in 3D bar

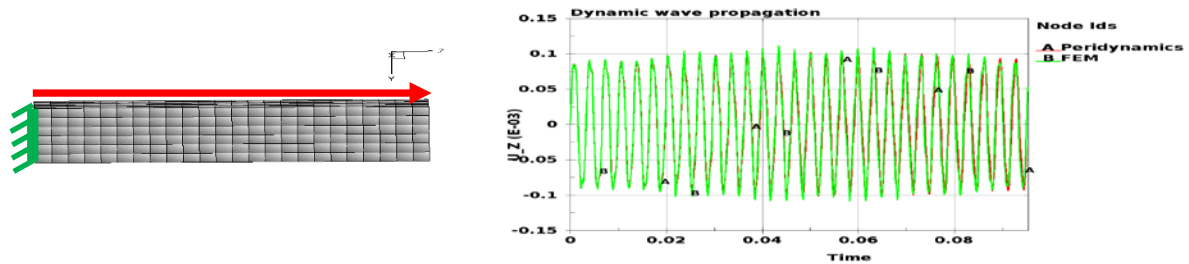


Fig. 3. The wave propagation in 3D bar. (a) specimen; (b) the displacement history of the middle point

In dynamic simulations, the stress wave plays a crucial role which induces all the material responses. The peridynamics applications run without stress status. However, the displacement of a particle is an alternative way to represent the waves inside a solid. A 3D elastic bar ($1.0m \times 1.0m \times 4.0m$) is subjected the initial velocity $V_z = 0.2 m/s$ in the whole specimen and fixed one end, shown as Fig. 3 (a). The material constants are $\rho = 8.0E3 kg/m^3$, $E = 190Gpa$. The specimen is discretized by 864 brick elements (8 nodes elements). This problem is carried out by the proposed method as well as the classic FEM method with the same elastic constants and $\nu = 0.25$. Induced by the initial velocity, the elastic specimen oscillates with time along the dynamic wave. The results from the bond-based peridynamics model and the classic FEM are compared in Fig 3 (b) with the displacement component u_z of the particle located at middle of the domain. Fig. 3 shows the almost identical curves from peridynamics and FEM which implies the proposed model can capture the dynamic response of material as FEM without the material failure.

6.2 The convergence of mode-I fracture

In this numerical examples, a rectangular sample ($0.1 m \times 0.2 m \times 0.03 m$) with two pre-cracks are stretched (velocity : $1.0 m/s$) at two ends with opposite directions as shown in Fig. 4. Consequently a mode-I crack will initiate and propagate along the initial cracks. The material constants used in this example are: $\rho = 8.0E3 kg/m^3$ $E = 190 Gpa$ $G = 5.5E4 J/m^2$. Three model refinements with 600,

4800, and 38400 elements are utilized to study the convergence of the proposed equations respectively.

The crack lengths of three refinements are compared in Fig. 5. Note the crack length is measured as an approximate value according the time sequence in the damage fringe plots shown in Fig. 6. In Fig. 5, the crack nucleation time are about the same (the maximum error: 2.0×10^{-5} s) with different refinements. Stable crack propagation is observed in three mesh models and the curves converge to the finest mesh model. It is interesting to note that the time-crack length curves of three refinements are nearly parallel which imply the same crack propagation speed in different meshes.

The damage morphologies of three refinements at $t = 420 \mu\text{s}$ are shown in Fig. 6. Here the fringe color represents the value of damage indicator according to Eq. 10. From Fig.8, one can observe that the damage is localized along the crack surface which resembles the mode-I failure in brittle material.

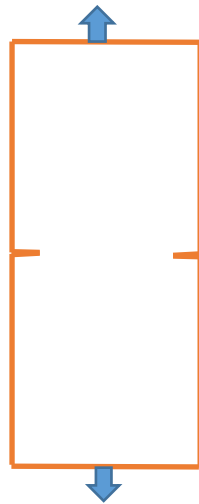


Fig. 4. The specimen with preset notches

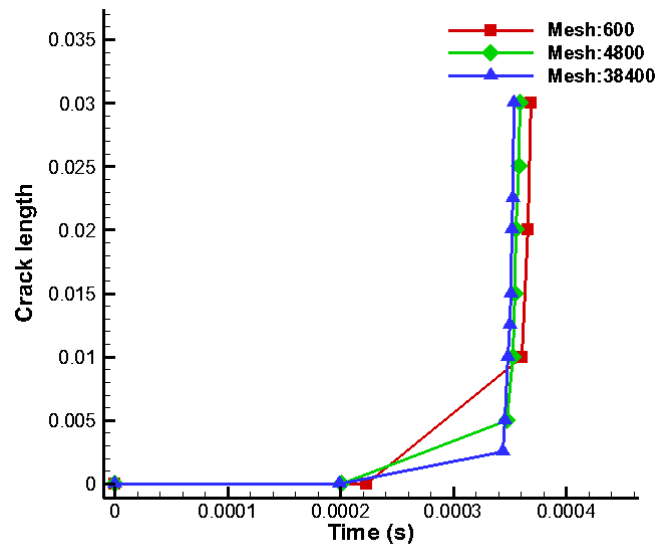


Fig. 5. The convergence of mode I fracture

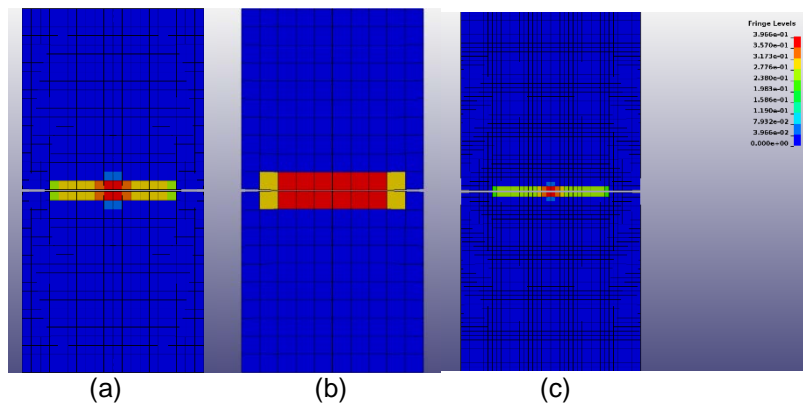


Fig. 6. The damage morphologies of mode I fracture, (a) coarse mesh (600 elements), (b) medium mesh (4800 elements), (c) fine mesh (38400 elements)

6.3 The Kalthoff-Winkler problem

In addition to the numerical advantages of boundary condition; contact/constraint enforcements; spatial integration of non-uniform mesh, coupling with other Galerkin-based numerical methods are embedded in the present method. There is a shortcoming introduced by the mesh-based integration: the crack path only goes along the edges of elements which result in some degrees of mesh dependence of crack path when the mesh is overly coarse. In this example, the Kalthoff-Winkler problem [14] which has two tilted cracks is carried out to study the sensitivity of crack propagation path in different mesh size.

The Kalthoff-Winkler experiment concerns the impact of a steel plate with two notches by a cylindrical impactor, Fig. 7. The diameter of the cylindrical impactor is 0.05 m with the mass of 1.57 kg . This simulation considers the impactor as rigid body. To reduce the computational cost, the impactor is represented by a rectangle shell structure with the same mass and interacts with the steel plate

through contact. The material constants of the specimen are listed: $\rho = 8.0E3 \text{ kg/m}^3$ $E = 190 \text{ Gpa}$ $G = 6.0E4 \text{ J/m}^2$. To study the convergence of the solution, the specimen is discretized with three refinements: the coarse mesh with 30800 elements, the medium mesh with 52272 elements and fine mesh with 97608 elements.

The history of crack length in three mesh refinements is shown in Fig. 8 which indicates a convergence of the solution. The time sequences of the failure process with different meshes are illustrated in Fig. 9 with the contour of damage indicator. While the main crack path in three mesh models has the angle about 68° as seen in the experimental results, the result of coarse mesh with 30800 elements predicts the secondary cracks. These secondary cracks do not shown up in the result of two refined mesh models, which is a consequence of equation (9), i.e., the coarser mesh results in a smaller critical bond stretch. This result suggests that the discretization of the FEM peridynamics model should be relatively refined in order to prevent the mesh size sensitivity and achieved the desired accuracy. However, the convergent solution is expected when the discretization model is continuously refined as shown in Fig 9 (g)-(i).

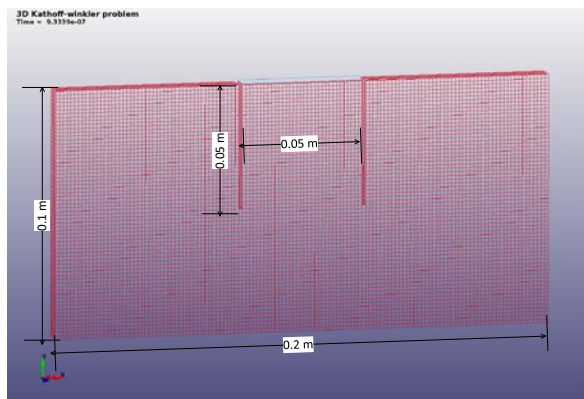


Fig. 7. Kalthoff-Winkler problem

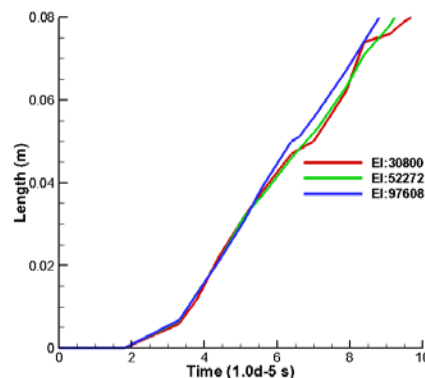


Fig. 8. The crack length history

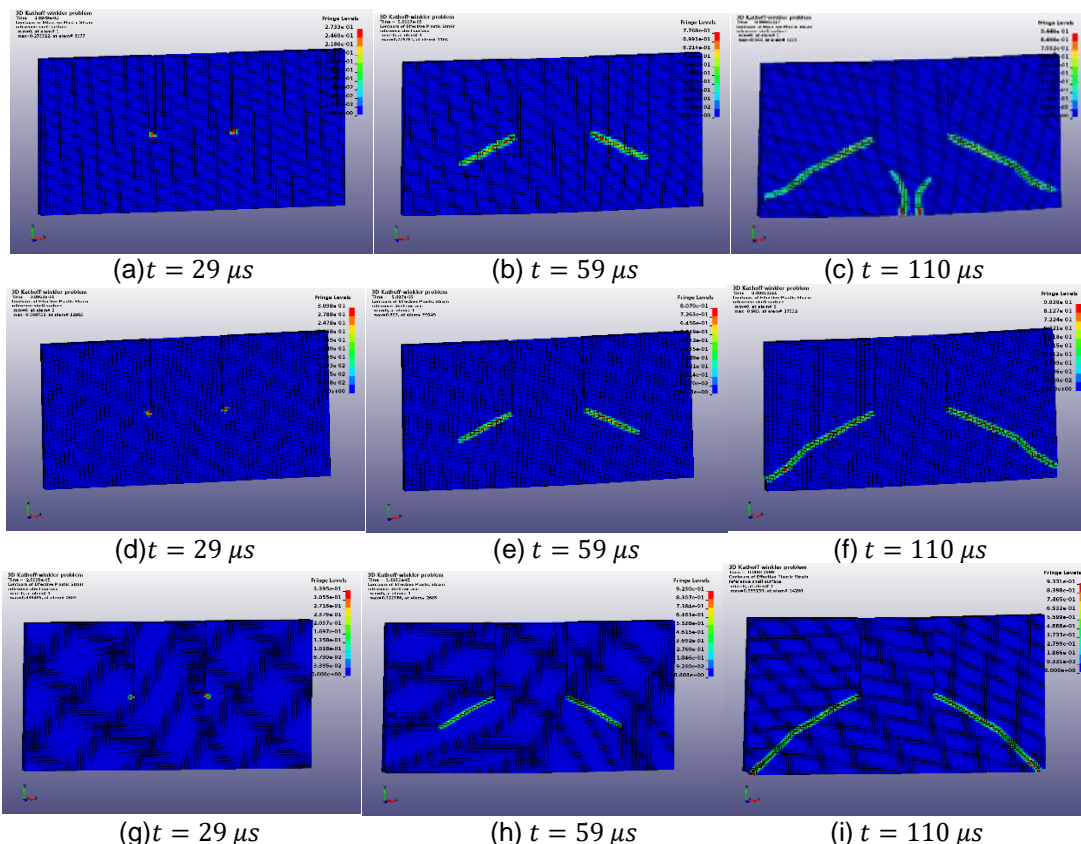


Fig. 9. The time sequence of damage process, background: damage indicator, (a)-(c): the coarse mesh; (d)-(f): medium mesh; (g)-(i): fine mesh

6.4 Mixed mode fracture in the three point bending problems

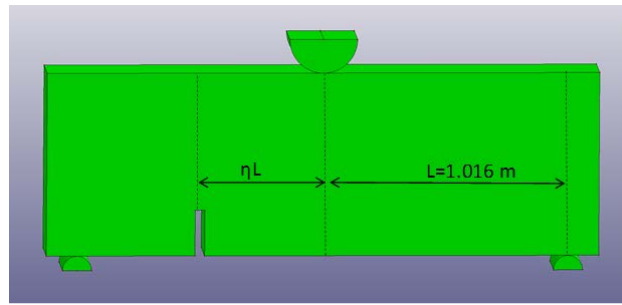


Fig. 10. The configuration of three point bending test

In this simulation, the three point bending tests of a pre-notched concrete beam are carried out. The configuration of the specimen and the position of notch are shown in Fig. 10 as the experimental set up [28]. The dimension of the specimen is $228.6\text{mm} \times 76.2\text{mm} \times 25.4\text{mm}$ supported by two fixed cylinders (radio: 6mm). The specimen is impacted by a cylinder projector with initial velocity: 0.05m/s . According to the different position of notches (height: 19.05mm), there are 3 cases of simulation are carried out which represent the mode-I fracture ($\eta = 0$ in Fig. 10) and the mixed mode fractures ($\eta = 0.5$ and $\eta = 0.7$) respectively. The material properties of concrete are: $E = 29\text{Gpa}$, $\rho = 2400\text{kg/m}^3$ and Fracture energy release rate: $G = 31.1\text{J/m}^2$. The two support cylinders and the impactor are considered as the rigid bodies. The specimen is partitioned by 27800 elements in each case. With different notch positions, the experimental tests show the tilted cracks with different angles, as Fig. 11. The case with $\eta = 0$ shows vertical crack and the cases ($\eta = 0.5$ and $\eta = 0.7$) have the tilted crack path with angle: ($\theta = 22^\circ$ and $\theta = 30^\circ$) respectively. The numerical simulations of these cases are plotted in Fig. 12 which illustrate a similar crack pattern with the angle 0° for $\eta = 0$; 21° for $\eta = 0.5$ and 29° for $\eta = 0.7$. This validation shows that the present method captures the fracture pattern well for the mode I and mixed modes.



Fig. 11. Experimental crack paths under impaction [28]

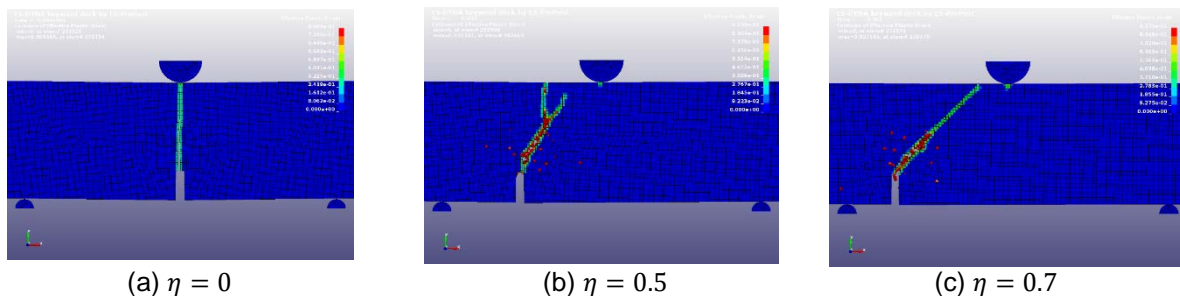


Fig. 12. The numerical predicted crack paths

6.5 Impact damage on the glass-polycarbonate-glass structure

One of the major applications of the bond-based peridynamics which concerns the brittle material is the damage prediction of windshield in the crashworthiness simulation. In contrast to the house windows, the automobile windshield is made of a three-layer structure (glass-polycarbonate (pc)-glass) as shown in Fig. 13. Hu et al. [25] reported their research on the experimental and numerical damage prediction of glass-PC structure using the standard bond-based peridynamics. Bobaru et al. [26] presented the numerical prediction of glasses-pc system where 7 glass layers stack on one PC layer. This numerical example follows most of their experimental settings and the material constants

except another glass layer is attached on the bottom of the PC layer, i.e., the specimen becomes a glass-PC-glass structure as shown in Fig. 13. In the experiment, the glass layers are clamped by a metal frame with a square hole of $5.08\text{ cm} \times 5.08\text{ cm}$. As shown in the study by Hu et al. [25] and Bobaru et al. [26], this clamp contact boundary condition is simplified as the fixed out-of-plane boundary condition in the contact zone (Fig 13, the red ring at the top and bottom surface). The glass is soda-lime glass with material properties given by: $\rho = 2.44E3\text{ kg/m}^3$, $E = 72Gpa$, $G = 8.0\text{ J/m}^2$ [25]. The projectile is treated as a rigid body with material constants given by $\rho = 3.73E3\frac{\text{kg}}{\text{m}^3}$, $E = 210Gpa$, $\nu = 0.3$. This density leads to a total mass of 0.692 g for projector. The projector is placed nearby the middle of the top surface with the initial velocity: $V_z = -31.0\text{ m/s}$. Because no damage is observed in the PC layer from experiments [25], the PC layer is considered a simple elastic material with $\rho = 1.2E3\text{ kg/m}^3$, $E = 2.0Gpa$, $\nu = 0.25$. There is no adhesive between glasses and PC layers in the experiments. Therefore, no cohesive elements are placed in the glass-PC and PC-glass interfaces for this numerical study. Instead, contacts are assumed in these interfaces and the projector-glass interface (the red surfaces in the middle of Fig. 13). The glass-PC-glass specimen is discretized by 100,000 elements for glasses, 2500 elements for PC layer and the projector is simulated by one layer of brick elements at surface with 1014 elements shown in Fig. 13.

The damage patterns of the specimen are shown in Fig 14. Most damage patterns observed in the experiment are reproduced in this numerical simulation: the ripple cracks in the ellipses, the splitting cracks in the circles, through-thickness tilted cracks in the diamonds and boundary cracks in triangles. On the top surface of the glass, the main failure pattern consists of diagonal cracks and circle cracks nearby the impact zone. At the bottom surface, there is a main damage circle zone and the diagonal cracks extend from this zone as shown Figs. 14 (a) and (b). This damage pattern is well recognized in the failure analysis of windshield applications. The section damage pattern of the glass-PC-glass system is shown in Fig. 15 where a clear cone shape damage zone which is found in other glass indentation experiments [27] is observed using the proposed method. The contact reaction force reacting on the projector is presented in Fig 16. The dynamic damage process is shown in Fig 17 where all the complex damage phenomena, such as the multi-cracks nucleation, cracks propagation, cracks bifurcation and cracks coalescence can be observed.

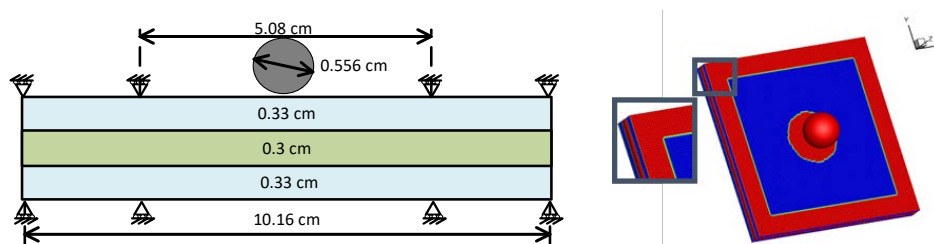


Fig. 13. The glass-PC-glass structure and computational model

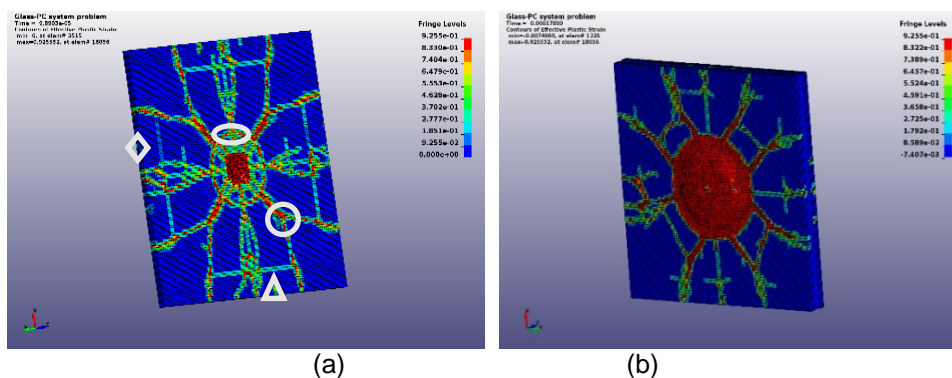


Fig. 14. The damage status by impaction, (a) the top surface; (b) the bottom surface

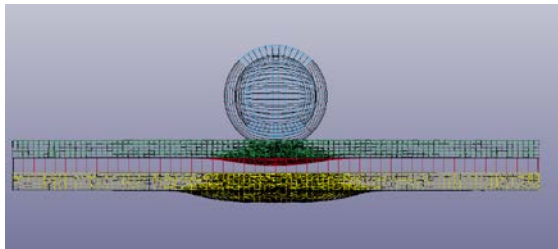


Fig. 15. The cone shape in global damage zone

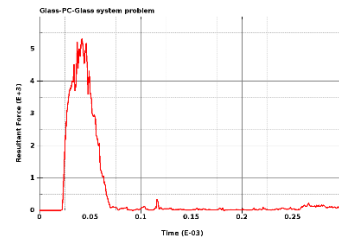
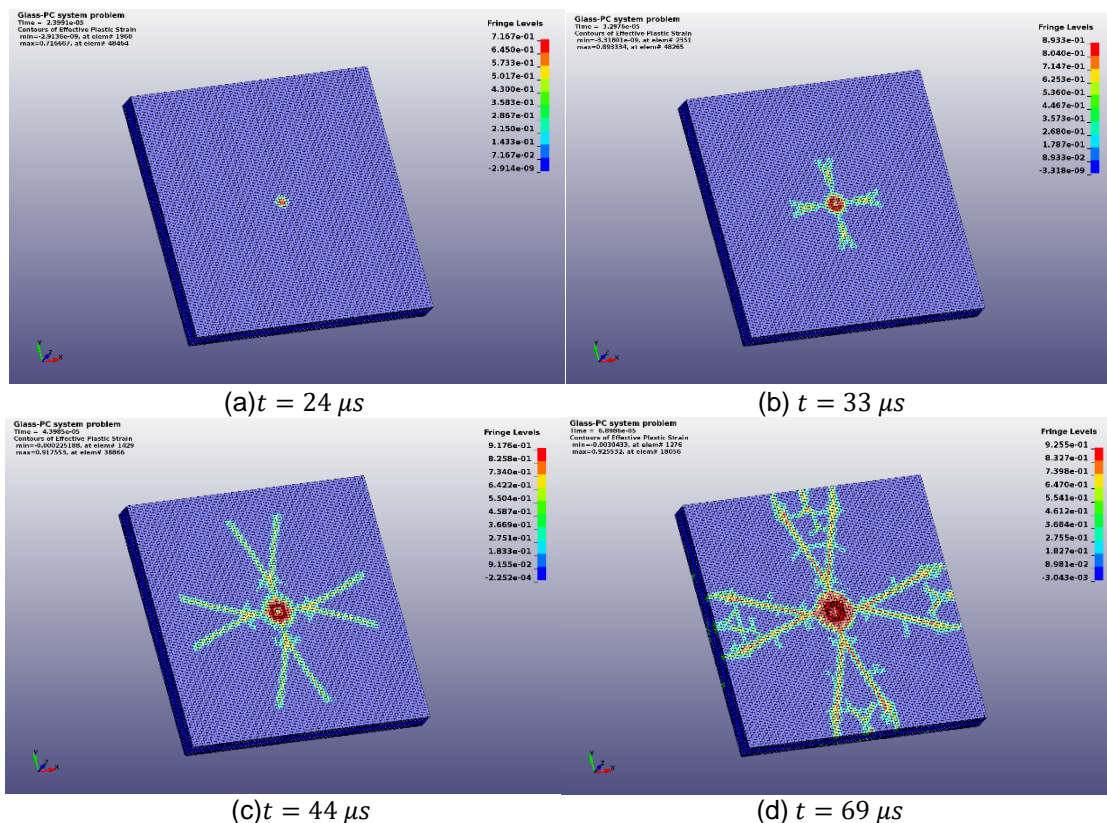


Fig. 16. The contact force

7 Summary

This paper presents the explicit dynamic formulas and numerical algorithms of bond-based peridynamics model to predict the damage of 3D brittle material. In contrast to the meshfree version of peridynamics, the discontinuous Galerkin weak form of the peridynamics dynamic governing equations is considered. The weak equation consists of two-levels of spatial integrations: the computational domain integration and horizon integration. In order to represent the moving strong discontinuities in the dynamic damage process, the solution is approximated as the element-wise discontinuous field by the regular FEM shape function. There are several practical usages to implement the bond-based peridynamics model in the FEM framework. First, the boundary condition enforcement is straightforward because the FEM shape functions satisfy the Kronecker-delta property. Second, the Gaussian integration can reduce the mesh dependence in the case of non-uniform mesh. Third, the mesh-based calculation represents the material boundary explicitly. Fourth, it's easy to utilize the existing contact algorithms to provide the contacts between peridynamics and FEM parts.



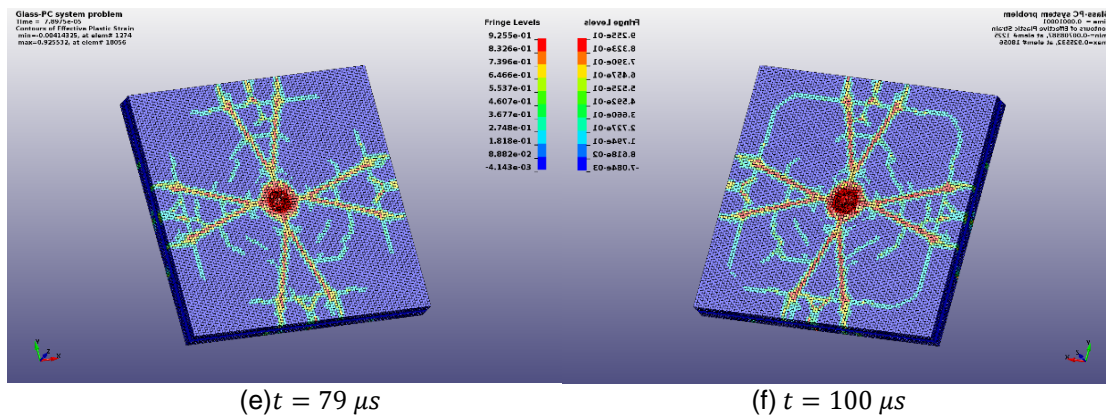


Fig. 17. The time sequence of damage process, background: damage indicator

As a nonlocal model, the numerical procedure presented in this paper considers the non-uniform discretization as well as the global boundary effect. The present numerical procedure was implemented to calculate the specific micro elastic modulus for each particle to assure the equivalent elastic energy density obtained by the classic mechanics theory. Therefore the non-failure material constant of the PMB material in this paper requires the classic elastic modulus E instead of the micro elastic modulus c . This paper uses the classic energy release rate as failure criteria which determines the critical bond stretch based on the equivalent energy to form a crack surface.

Several numerical examples are carried out to study the performance of the proposed method. The results suggest that this method can capture the dynamic response of elastic solid by the classic FEM method before damage occurs. The method can also predict the 3D dynamic process of mixed modes fracture, multi-cracks fracture and fragmentation effectively and accurately during the damage process.

8 Acknowledgment

The authors wish to thank Dr. John O. Hallquist of LSTC for his support to this research. Helpful discussions with Dr. Stewart Silling and Dr. David John Littlewood of Sandia National Laboratories, Dr. Gilles Lubineau and Dr. Fei Han from King Abdullah University of Science and Technology, and Dr. Hamid Razi from Boeing Company are gratefully acknowledged.

9 Literature

- [1] Moës N, Dolbow J, Belytschko T. A finite element method for crack growth without remeshing. *International Journal for Numerical Methods in Engineering* 1999;46: 133–150.
- [2] Xu XP, Needleman A. Numerical simulations of fast crack growth in brittle solids. *Journal of the Mechanics and Physics of Solid* 1994;42:1397–1434.
- [3] Ren B, Li SF. Modeling and simulation of large-scale ductile fracture in plates and shells. *International Journal of Solids and Structures* 2012;49: 2373–2393.
- [4] Kroner E. Elasticity theory of materials with long range forces. *Int J Solids Struct* 1967;3:731-742.
- [5] Chen JS, Wu CT, Belytschko T. Regularization of material instabilities by meshfree approximations with intrinsic length scales. *Int J Numer Methods Eng* 2000;47:1303-1322.
- [6] Silling SA. Reformulation of elasticity theory for discontinuities and long-range forces. *Journal of the Mechanics and Physics of Solids* 2000;48:175-209.
- [7] Silling SA, Epton M, Weckner O, Xu J, Askari E. Peridynamics states and constitutive modeling. *J Elast* 2007;88:151-184.
- [8] Bobaru F, Hu W. The meaning, selection, and use of the peridynamics horizon and its relation to crack branching in brittle materials. *International Journal of Fracture* 2012;176:215–222.
- [9] Gerstle W, Sau N, Silling SA. Peridynamic modeling of concrete structures. *Nuclear Engineering and Design* 2007;237:1250–1258.
- [10] Askari E, Xu J, Silling S. Peridynamic analysis of damage and failure in composites. 44th AIAA Aerospace Sciences Meeting and Exhibit, Reno, Nevada, 2006;1–12.
- [11] Kilic B, Madenci E, Ambur DR. Analysis of brazed single-lap joints using the peridynamics theory. 47th AIAA/ASME/ASCE/AHS/ASC Structures, Structural Dynamics, and Materials Conference, Newport, Rhode Island, 2006;1.

- [12] Lai X, Ren B, Fan HF, Li SF, Wu CT, Regueiro RA, Liu LS. Peridynamics simulations of geomaterial fragmentation by impulse loads. *Int J Numer Anal Meth Geomech* 2015;39:1304–1330.
- [13] Warren TL, Silling SA, Askari A, Weckner O, Epton MA, Xu J. A non-ordinary state-based peridynamic method to model solid material deformation and fracture. *International Journal of Solids and Structures* 2009;46:1186–1195.
- [14] Madenci E, Oterkus E. *Peridynamic Theory and Its Applications*. Springer, New York, 2014.
- [15] Wu CT. Kinematic constraints in the state-based peridynamics with mixed local/nonlocal gradient approximations. *Computational Mechanics* 2014;54: 1255-1267.
- [16] Wu CT, Ren B. A stabilized non-ordinary state-based peridynamics for the nonlocal ductile material failure analysis in metal machining process. *Computer Methods in Applied Mechanics and Engineering* 2015;291:197-215.
- [17] Silling SA, Askari E. A meshfree method based on the peridynamic model of solid mechanics. *Computers and Structures* 2005;83:1526–1535.
- [18] Macek RW, Silling SA. Peridynamics via finite element analysis. *Finite Elements in Analysis and Design* 2007;43:1169-1178.
- [19] Chen X, Gunzburger M. Continuous and discontinuous finite element methods for a peridynamics model of mechanics. *Comput Methods Appl Mech Engrg* 2011;200:1237-1250.
- [20] Du Q, Zhou K. Mathematical Analysis for the peridynamic nonlocal continuum theory. *ESAIM: Mathematical Modelling and Numerical Analysis* 2011;45: 217-234.
- [21] Zhou K, Du Q. Mathematical and numerical analysis of linear peridynamic models with Nonlocal Boundary conditions. *SIAM J NUMER ANAL* 2010;48(5):1759-1780.
- [22] Lubineau G, Azdoud Y, Han F, Rey C, Askari A. A morphing strategy to couple non-local to local continuum mechanics. *Journal of the Mechanics and Physics of Solids* 2012;60:1088-1102.
- [23] Azdoud Y, Han F, Lubineau G. The morphing method as a flexible tool for adaptive local/non-local simulation of static fracture. *Comput Mech* 2014;54:711-722.
- [24] Shu CW. Discontinuous Galerkin method for time-dependent problems: survey and recent developments, chapter in *Recent Developments in Discontinuous Galerkin Finite Element Methods for Partial Differential Equations*. Springer, New York, 2013.
- [25] Hu W, Wang Y, Yu J, Yen CF, Bobaru F. Impact damage on a thin glass plate with a thin polycarbonate backing. *International Journal of Impact Engineering* 2013;62:152-165.
- [26] Bobaru F, Ha YD, Hu W. Damage progression from impact in layered glass modeled with peridynamics. *Central European Journal of Engineering* 2012;2(4):551-561.
- [27] Benbow J. Cone Cracks in Fused Silica. *Proceedings of the Physical Society* 1959;75(5): 697-699.
- [28] Reji J, Surendra PS. Mixed-mode fracture of concrete subjected to impact loading. *J Struct Eng* 1990;116(3):585-602.
- [29] Ghajari M, Iannucci L, Curtis P. A Peridynamic Material Model for the Analysis of Dynamic Crack Propagation in Orthotropic Media. *Computer Methods in Applied Mechanics and Engineering* 2014; 276(1):431:452.